

BOUT++ simulation study of turbulence transport during *n*=4 resonant magnetic perturbation induced edge localized mode suppression phase in EAST

Ziming Zhen(甄子明), Taihao Huang(黄泰豪), Yuchen Xu(徐宇晨), Hui Sheng(盛回), Tianyuan Liu(刘天元), Xueruoqi Liang(梁雪若棋), Manni Jia(贾曼妮), Xuemin Wu(吴学民), Shifeng Mao(毛世峰), Yanlong Li(李彦龙), Tianyang Xia(夏天阳), Youwen Sun(孙有文), and Minyou Ye(叶民友)

Citation: Chin. Phys. B, 2026, 35 (**4**): 045201. DOI: 10.1088/1674-1056/ae04d8
http://cpb.iphy.ac.cn; http://iopscience.iop.org/cpb

What follows is a list of articles you may be interested in

Discrete Alfvén eigenmodes in the CFETR steady-state scenario

Yuan-Dan Lan(兰源丹), Shuang-Hui Hu(胡双辉), Si-Jie Ouyang(欧阳思杰),Wan-Po Zhu(朱万坡), and Xuan-Ge Huang(黄旋格)

Chin. Phys. B, 2023, 32 (**5**): 055201. DOI: 10.1088/1674-1056/aca397

Experimental investigation on divertor tungsten sputtering with neon seeding in ELMy H-mode plasma in EAST tokamak

Dawei Ye(叶大为), Fang Ding(丁芳), Kedong Li(李克栋), Zhenhua Hu(胡振华), Ling Zhang(张凌), Xiahua Chen(陈夏华), Qing Zhang(张青), Pingan Zhao(赵平安), Tao He(贺涛), Lingyi Meng(孟令义), Kaixuan Ye(叶凯萱), Fubin Zhong(钟富彬), Yanmin Duan(段艳敏), Rui Ding(丁锐), Liang Wang(王亮), Guosheng Xu(徐国盛), Guangnan Luo(罗广南), and EAST team

Chin. Phys. B, 2022, 31 (**6**): 065201. DOI: 10.1088/1674-1056/ac4f58

Simulation of helium supersonic molecular beam injection in tokamak plasma

Xue-Ke Wu(吴雪科), Zhan-Hui Wang(王占辉), Hui-Dong Li(李会东), Li-Ming Shi(石黎铭), Di Wan(万迪), Qun-Chao Fan(樊群超), Min Xu(许敏)

Chin. Phys. B, 2020, 29 (**6**): 065201. DOI: 10.1088/1674-1056/ab81fd

Estimation of tungsten production from the upper divertor in EAST during edge localized modes

Jing Ou(欧靖), Nong Xiang(项农), Zong-Zheng Men(门宗政), Ling Zhang(张凌), Ji-Chan Xu(许吉禅), Wei Gao(高伟)

Chin. Phys. B, 2019, 28 (**12**): 125201. DOI: 10.1088/1674-1056/ab5279

Simulations of the L–H transition dynamics with different heat and particle sources

Li Hui-Dong (李会东), Wang Zhan-Hui (王占辉), Jan Weiland, Feng Hao (冯灏), Sun Wei-Guo (孙卫国)

Chin. Phys. B, 2015, 24 (**11**): 115204. DOI: 10.1088/1674-1056/24/11/115204

BOUT++ simulation study of turbulence transport during $n = 4$ resonant magnetic perturbation induced edge localized mode suppression phase in EAST

Ziming Zhen(甄子明)[1], Taihao Huang(黄泰豪)[1], Yuchen Xu(徐宇晨)[1], Hui Sheng(盛回)[2], Tianyuan Liu(刘天元)[1], Xueruoqi Liang(梁雪若棋)[1], Manni Jia(贾曼妮)[2], Xuemin Wu(吴学民)[1,2], Shifeng Mao(毛世峰)[1,†], Yanlong Li(李彦龙)[2], Tianyang Xia(夏天阳)[2], Youwen Sun(孙有文)[2], and Minyou Ye(叶民友)[1,‡]

[1] *School of Nuclear Science and Technology, University of Science and Technology of China, Hefei* 230026, *China*
[2] *Institute of Plasma Physics, Chinese Academy of Sciences, Hefei* 230031, *China*

(Received 27 April 2025; revised manuscript received 12 August 2025; accepted manuscript online 9 September 2025)

The effect of the resonant magnetic perturbation (RMP) on the turbulence transport during the edge localized mode (ELM) suppression phase is investigated by the BOUT++ six-field two-fluid simulations. Based on the edge plasma profiles during the ELM suppression phase in EAST experiment with $n = 4$ RMP (n is the toroidal mode number), the plasma response field is calculated using CLTx and introduced in the BOUT++ simulation. Compared with the case without RMP, the simulated flux-surface averaged radial particle flux at the position of peak pressure gradient increases to ~ 1.5 times for the case with RMP, which is close to the estimated particle flux according to the experimental plasma profiles. It implies that the turbulence transport could have a dominating contribution to the radial transport for maintaining the pedestal density profile during ELM suppression phase after density pump-out, especially when the stochasticity of the magnetic field is not significant in the pedestal region. The increase in the radial particle flux for the case with RMP is due to the significant increase in electric drift flux, which is partly offset by the magnetic flutter flux. The enhancement of the turbulent electric drift flux is mainly due to the enhanced density and electric potential perturbations. The change in the phase difference between them further enhances the contributions of the medium-n modes and suppresses the contribution of the low-n modes. Further complexity–entropy analysis indicates that the turbulence is more stochastic, which could be related to the enhanced mode-mode coupling due to RMP effect.

Keywords: pedestal, resonant magnetic perturbation, density pump-out, turbulent transport, BOUT++

PACS: 52.35.Ra, 52.25.Gj, 52.30.–q

DOI: 10.1088/1674-1056/ae04d8 **CSTR:** 32038.14.CPB.ae04d8

1. Introduction

In tokamak devices, the burst of edge localized modes (ELMs) can lead to extremely high heat loads on divertor targets. The resonant magnetic perturbation (RMP) has been demonstrated as an effective way of controlling ELMs in various tokamaks, including EAST,[1] DIII-D,[2] ASDEX-Upgrade,[3,4] and KSTAR.[5] The RMP-induced ELM suppression is often accompanied by a density pump-out effect,[6–8] characterized by a flattening of the density profile and enhanced radial transport. It is important to understand the mechanism of the density pump-out phenomenon due to its effects on edge plasma stability and confinement performance.

Several mechanisms have been proposed to explain this phenomenon. The change in the magnetic topology, i.e., forming magnetic islands in the pedestal region or creating stochastic magnetic fields at the edge due to the RMP, can enhance radial particle transport.[9,10] The neoclassical toroidal viscosity (NTV) effect, which is induced by the toroidal asymmetry of the magnetic field, can also affect radial transport.[11] It has also been indicated that a strong correlation exists between the edge kink/peeling response and density pump-out during ELM suppression.[12,13]

It is also found in the experiments that the enhanced turbulent transport also contributes to the density pump-out. In EAST experiments, the enhancement of perturbations has been observed and is considered due to a reduction in the $E \times B$ shear rate caused by the RMP-induced magnetic stochasticity.[6] In further experiments, the enhancement of radial particle transport, together with significant enhancement of edge turbulence, was observed during the RMP-induced ELM suppression phase.[14] For DIII-D,[15,16] the application of RMP led to ELM suppression, with a widespread enhancement of turbulence in the region of the normalized minor radius larger than 0.6. In ASDEX Upgrade experiments, broadband density perturbations are observed when the RMP field strength is below a certain threshold and a narrow-band quasi-

†Corresponding author. E-mail: sfmao@ustc.edu.cn
‡Corresponding author. E-mail: yemy@ustc.edu.cn

© 2026 Chinese Physical Society and IOP Publishing Ltd. All rights, including for text and data mining, AI training, and similar technologies, are reserved.

coherent mode appears above the threshold,[8] which can significantly enhance radial particle transport and cause the density pump-out.

BOUT++ code[17] has been widely employed for numerical simulations of edge plasma turbulence. Kim *et al.* explored the influence of RMP fields on pedestal collapse using the three-field model and revealed that the RMP-mediated nonlinear interaction enhanced the perturbation level, leading to an increase in convective transport.[18] Dong *et al.* investigated the effects of RMP fields on peelingballooning (PB) modes based on the four-field model and revealed that RMP can reduce linear growth rates by directly coupling with PB modes and enhance multi-mode coupling in the nonlinear process.[19–21] Based on the six-field two-fluid model, Deng *et al.* found that the transport coefficient is larger for the EAST edge plasma after RMP-induced density pump-out.[22] However, the effect of perturbation fields on the turbulence transport for the edge plasma after density pump-out is still not clear.

In this work, by introducing the response field into the BOUT++ simulation based on the six-field two-fluid model, the effect on the turbulence transport during RMP-induced ELM suppression phase is investigated. The rest of this paper is organized as follows. In Section 2, the method for introducing the perturbation field in the BOUT++ six-field two-fluid model is stated, where the response field induced by RMP is calculated using CLTx[9,23] based on the equilibrium from the EAST experiment.[1,24] Section 3 compares the simulated radial particle fluxes with and without RMP and investigates the mechanism of the enhancement of turbulence transport. The summary is given in Section 4.

2. Simulation model and setup

2.1. BOUT++ simulation model with a perturbation field

BOUT++ is a three-dimensional (3D) fluid code primarily used for numerical simulation of edge plasma turbulence. The model used in this paper is based on the six-field two-fluid model developed by Xia *et al.*[25] as follows:

$$\begin{aligned}\frac{\partial \varpi}{\partial t} =& -\frac{1}{B_0}\boldsymbol{b}\times\boldsymbol{\nabla}_\perp\Phi\cdot\boldsymbol{\nabla}\varpi + B_0^2\nabla_\parallel\left(\frac{J_\parallel}{B_0}\right) + 2\boldsymbol{b}\times\boldsymbol{\kappa}\cdot\boldsymbol{\nabla}P_\mathrm{i}\\ &-\frac{1}{2\Omega_\mathrm{i}}\left[\frac{1}{B_0}\boldsymbol{b}\times\boldsymbol{\nabla}P_\mathrm{i}\cdot\nabla\left(\nabla_\perp^2\Phi\right) - Z_i e B_0\boldsymbol{b}\times\boldsymbol{\nabla}n_\mathrm{i}\cdot\boldsymbol{\nabla}\left(\frac{\nabla_\perp\Phi}{B_0}\right)^2\right]\\ &+\frac{1}{2\Omega_\mathrm{i}}\left[\frac{1}{B_0}\boldsymbol{b}\times\boldsymbol{\nabla}\Phi\cdot\boldsymbol{\nabla}\left(\nabla_\perp^2 P_\mathrm{i}\right) - \nabla_\perp^2\left(\frac{1}{B_0}\boldsymbol{b}\times\boldsymbol{\nabla}\Phi\cdot\boldsymbol{\nabla}P_\mathrm{i}\right)\right] + \mu_{\parallel\mathrm{i}}\nabla_{\parallel 0}^2\varpi, \end{aligned} \tag{1}$$

$$\frac{\partial n_\mathrm{i}}{\partial t} = -\frac{1}{B_0}\boldsymbol{b}\times\boldsymbol{\nabla}_\perp\Phi\cdot\boldsymbol{\nabla}n_\mathrm{i} - \frac{2n_\mathrm{i}}{B_0}\boldsymbol{b}\times\boldsymbol{\kappa}\cdot\boldsymbol{\nabla}\Phi - \frac{2}{Z_\mathrm{i}eB_0}\boldsymbol{b}\times\boldsymbol{\kappa}\cdot\boldsymbol{\nabla}P_\mathrm{i} - n_\mathrm{i}B_0\nabla_\parallel\left(\frac{V_{\parallel\mathrm{i}}}{B_0}\right), \tag{2}$$

$$\frac{\partial V_{\parallel\mathrm{i}}}{\partial t} = -\frac{1}{B_0}\boldsymbol{b}\times\boldsymbol{\nabla}_\perp\Phi\cdot\boldsymbol{\nabla}V_{\parallel\mathrm{i}} - \frac{1}{m_\mathrm{i}n_{\mathrm{i}0}}\boldsymbol{b}\cdot\boldsymbol{\nabla}P, \tag{3}$$

$$\frac{\partial A_\parallel}{\partial t} = -\nabla_\parallel\phi + \frac{\eta}{\mu_0}\nabla_\perp^2 A_\parallel + \frac{1}{en_{\mathrm{e}0}B_0}\nabla_\parallel P_\mathrm{e} + \frac{0.71k_\mathrm{B}}{eB_0}\cdot\nabla_\parallel T_\mathrm{e} - \frac{\eta_\mathrm{H}}{\mu_0}\nabla_\perp^4 A, \tag{4}$$

$$\begin{aligned}\frac{\partial T_\mathrm{i}}{\partial t} =& -\frac{1}{B_0}\boldsymbol{b}\times\boldsymbol{\nabla}_\perp\Phi\cdot\boldsymbol{\nabla}T_\mathrm{i} - \frac{2}{3}T_\mathrm{i}\left[\left(\frac{2}{B_0}\boldsymbol{b}\times\boldsymbol{\kappa}\right)\cdot\left(\boldsymbol{\nabla}\Phi + \frac{1}{Z_\mathrm{i}en_{\mathrm{i}0}}\boldsymbol{\nabla}P_\mathrm{i} + \frac{5}{2}\frac{k_\mathrm{B}}{Z_\mathrm{i}e}\boldsymbol{\nabla}T_\mathrm{i}\right) + B_0\nabla_\parallel\left(\frac{V_{\parallel\mathrm{i}}}{B_0}\right)\right]\\ &+\frac{2}{3n_{\mathrm{i}0}k_\mathrm{B}}\nabla_{\parallel 0}\left(\kappa_{\parallel\mathrm{i}}\nabla_{\parallel 0}T_\mathrm{i}\right) + \frac{2}{3n_{\mathrm{i}0}k_\mathrm{B}}\boldsymbol{\nabla}_\perp\cdot\left(\kappa_{\perp\mathrm{i}}\boldsymbol{\nabla}_\perp T_\mathrm{i}\right) + \frac{2m_\mathrm{e}}{m_\mathrm{i}}\frac{Z_\mathrm{i}}{\tau_\mathrm{e}}\left(T_\mathrm{e}-T_\mathrm{i}\right), \end{aligned} \tag{5}$$

$$\begin{aligned}\frac{\partial T_\mathrm{e}}{\partial t} =& -\frac{1}{B_0}\boldsymbol{b}\times\boldsymbol{\nabla}_\perp\Phi\cdot\boldsymbol{\nabla}T_\mathrm{e} - \frac{2}{3}T_\mathrm{e}\left[\left(\frac{2}{B_0}\boldsymbol{b}\times\boldsymbol{\kappa}\right)\cdot\left(\boldsymbol{\nabla}\Phi - \frac{1}{en_{\mathrm{e}0}}\boldsymbol{\nabla}P_\mathrm{e} - \frac{5}{2}\frac{k_\mathrm{B}}{e}\boldsymbol{\nabla}T_\mathrm{e}\right) + B_0\nabla_\parallel\left(\frac{V_{\parallel\mathrm{e}}}{B_0}\right)\right]\\ &+0.71\frac{2T_\mathrm{e}}{3en_{\mathrm{e}0}}B_0\nabla_\parallel\left(\frac{J_\parallel}{B_0}\right) + \frac{2}{3n_{\mathrm{e}0}k_\mathrm{B}}\nabla_{\parallel 0}\left(\kappa_{\parallel\mathrm{e}}\nabla_{\parallel 0}T_\mathrm{e}\right) + \frac{2}{3n_{\mathrm{e}0}k_\mathrm{B}}\boldsymbol{\nabla}_\perp\cdot\left(\kappa_{\perp\mathrm{e}}\boldsymbol{\nabla}_\perp T_\mathrm{e}\right) - \frac{2m_\mathrm{e}}{m_\mathrm{i}}\frac{1}{\tau_\mathrm{e}}\left(T_\mathrm{e}-T_\mathrm{i}\right) + \frac{2}{3n_{\mathrm{e}0}k_\mathrm{B}}\eta_\parallel J_\parallel^2. \end{aligned} \tag{6}$$

The definitions of ϖ, $J_\parallel$, and $V_{\parallel\mathrm{e}}$ are as follows:

$$\varpi = n_{\mathrm{i}0}\frac{m_\mathrm{i}}{B_0}\left(\nabla_\perp^2\phi + \frac{1}{n_{\mathrm{i}0}}\boldsymbol{\nabla}_\perp\phi\cdot\boldsymbol{\nabla}_\perp\phi + \frac{1}{n_{\mathrm{i}0}Z_\mathrm{i}e}\nabla_\perp^2 p_{\mathrm{i}1}\right), \tag{7}$$

$$J_\parallel = J_{\parallel 0} - \frac{1}{\mu_0}B_0\nabla_\perp^2\psi, \tag{8}$$

$$V_{\parallel\mathrm{e}} = V_{\parallel\mathrm{i}} + \frac{1}{\mu_0 Z_\mathrm{i}en_\mathrm{i}}\nabla_\perp^2 A_\parallel. \tag{9}$$

In the equations, all the variables F can be written as $F = F_0 + F_1$, where F_0 represents the equilibrium part and F_1 is the perturbed component. $A_\parallel$ is the parallel vector potential, $\boldsymbol{b} = \boldsymbol{b}_0 + \boldsymbol{b}_1 = \boldsymbol{b}_0 + \boldsymbol{\nabla}A_\parallel\times\boldsymbol{b}_0/B$ is the unit vector of the total magnetic field, $\boldsymbol{\kappa} = \boldsymbol{b}_0\cdot\nabla\boldsymbol{b}_0$. For j species, the pressure is $P_j = P_{j0} + p_{j1}$, and the perturbed pressure is $p_{j1} = n_{j0}T_{j1} + n_{j1}T_{j0} + n_{j1}T_{j1}$. $\Phi = \Phi_0 + \phi$ is the total electric potential, and $\boldsymbol{V}_E = (\boldsymbol{b}_0\times\boldsymbol{\nabla}_\perp\Phi)/B_0$. $\Omega_\mathrm{i} = Z_\mathrm{i}eB/m_\mathrm{i}$ is the ion gyro frequency, $\nabla_{\parallel 0} = \boldsymbol{b}_0\cdot\boldsymbol{\nabla}$, $\nabla_\parallel = \nabla_{\parallel 0} + \boldsymbol{b}_1\cdot\boldsymbol{\nabla}$, and

$\nabla_\perp = \nabla - \boldsymbol{b}\nabla_\parallel$.

The perturbation field induced by RMP $\boldsymbol{B}_{\rm RMP}$ is introduced in the simulation according to Dong *et al.*'s work.[19] Let $\boldsymbol{B}'_0$ be the sum of the toroidally symmetric magnetic field from the equilibrium $\boldsymbol{B}_0$ and $\boldsymbol{B}_{\rm RMP}$, i.e.,

$$\boldsymbol{B}'_0 = \boldsymbol{B}_0 + \boldsymbol{B}_{\rm RMP}. \tag{10}$$

Because the strength of the perturbation field is usually about 4 orders of magnitude lower than the equilibrium magnetic field, we have

$$B'_0 = \left|\boldsymbol{B}'_0\right| = \left|\boldsymbol{B}_0 + \boldsymbol{B}_{\rm RMP}\right| \approx \left|\boldsymbol{B}_0\right| = B_0, \tag{11}$$

$$\boldsymbol{b}'_0 = \frac{\boldsymbol{B}_0 + \boldsymbol{B}_{\rm RMP}}{B'_0} \approx \frac{\boldsymbol{B}_0}{B_0} + \frac{\boldsymbol{B}_{\rm RMP}}{B_0} = \boldsymbol{b}_0 + \frac{\boldsymbol{B}_{\rm RMP}}{B_0}, \tag{12}$$

where $\boldsymbol{b}'_0$ is the unit vector of $\boldsymbol{B}'_0$.

By substituting $\boldsymbol{b}_0$ in the original six-field two-fluid model by $\boldsymbol{b}'_0$ defined in Eq. (12), the effect of RMP can be introduced. In addition, for any physical quantity F, the parallel differential operator is also modified as

$$\nabla_{\parallel 0} F = \boldsymbol{b}_0 \cdot \nabla F + \frac{\boldsymbol{B}_{\rm RMP}}{B_0} \cdot \nabla F. \tag{13}$$

It should be noted that the above method is not the only way to introduce RMP fields. As described in Ref. [18,26], the RMP field is introduced by applying the external vacuum magnetic perturbation as the boundary condition of the magnetic potential. Furthermore, only the magnetic response field induced by the RMP is introduced in the present simulation model, while the perturbations of other physical quantities in CLTx (see Subsection 2.3) such as the pressure have not been taken into account. Moreover, the application of RMP would also affect the plasma rotation and therefore the equilibrium. To achieve a comprehensive understanding on the mechanism how the RMP affects the plasma turbulence, it is necessary to develop a more self-consistent simulation model in the future work.

2.2. Simulation setup

In EAST discharge #94048,[1,24,27] by applying $n = 4$ RMP (coil current 3 kA, with a 180° phase difference between the upper and lower coil sets), where n is the toroidal mode number, sustained ELM suppression for 1.8 s (5.2 s–7 s) is successfully achieved, as shown in Fig. 1. The equilibrium and edge plasma profiles at 5.9 s during the ELM suppression phase are used in the simulation study. Figure 2 shows the edge plasma profiles of pressure, electron density, electron temperature, and ion temperature at 5.9 s of EAST discharge #94048. The BOUT++ simulation region covers the pedestal and the scrape-off layer (SOL) for $\psi = 0.7$–1.05, where ψ is the normalized poloidal magnetic flux. The grid sizes are 256×64×64 in the (x, y, z) directions, as shown in Fig. 3. The X-point is excluded during the construction of the BOUT++ simulation grid,[28] which eliminates the difficulty in dealing with the poloidal magnetic field singularity. Due to limitation of computational resource, only 1/4 of the torus is simulated in this work. It should be noted that, this choice is also due to the toroidal mode number of RMP. The present BOUT++ simulation based on 1/4 torus cannot deal with the modes with $n = 1$–3. Therefore, if $n = 1$ RMP is applied, it will require a full-torus simulation.[29]

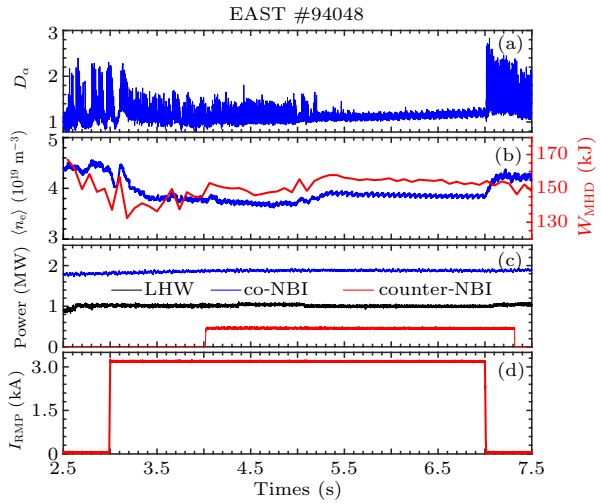


Fig. 1. Time evolution of different discharge parameters: (a) D_α signal, (b) line-averaged plasma density (blue) and plasma stored energy (red), (c) lower hybrid heating power (black), co-NBI heating power (blue), and counter-NBI heating power (red); (d) RMP coil current.

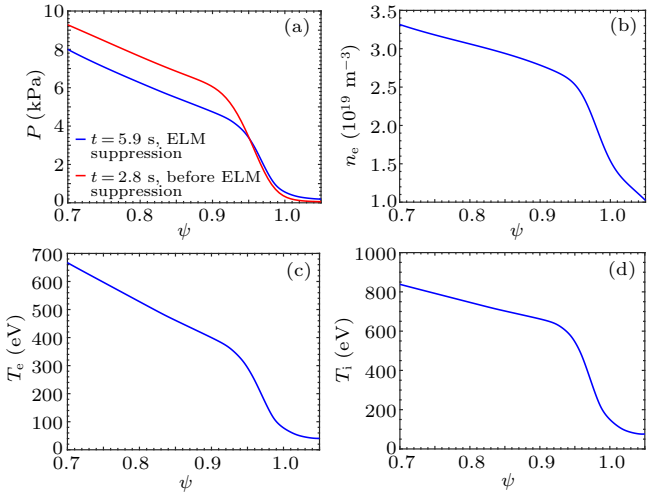


Fig. 2. Edge plasma profiles of (a) pressure, (b) electron density, (c) electron temperature, and (d) ion temperature. The blue lines indicate the profiles after ELM suppression, which are used in the BOUT++ simulations. The red line in panel (a) is the pressure profile before ELM suppression (not used for the BOUT++ simulation). The reduction in the pressure gradient after ELM suppression reflects the increase of radial transport.

Two cases, i.e., without RMP and with RMP, are simulated by BOUT++ and compared in Section 3 to investigate the influence due to RMP. Both cases are based on the same edge plasma profiles shown in Fig. 2 (blue lines) and same setups described above. In the case with RMP, the perturbation field, i.e., the plasma response field induced by RMP calculated using CLTx in Subsection 2.3, is introduced according

Eqs. (10)–(13), while in the case without RMP the perturbation field induced by RMP is not considered.

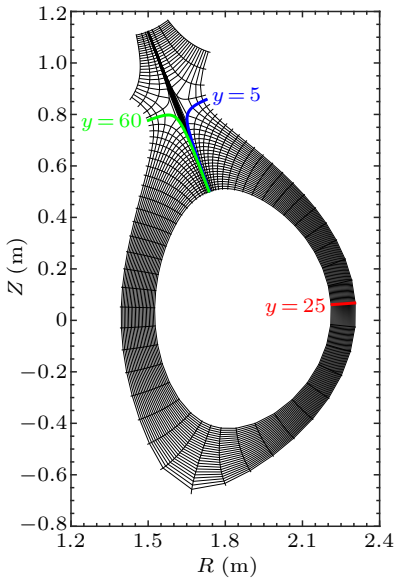


Fig. 3. BOUT++ simulation grid. Poloidal index $y = 25$ indicates the outer mid-plane.

2.3. RMP-induced response field

CLTx is an extended version of the cylindrical coordinate 3D magnetohydrodynamic code CLT (Ci–Liu–Ti, meaning MHD in Chinese).[30] In CLTx, the scrape-off layer can be self-consistently simulated, and an RMP module is developed for calculating the plasma response field to RMP.

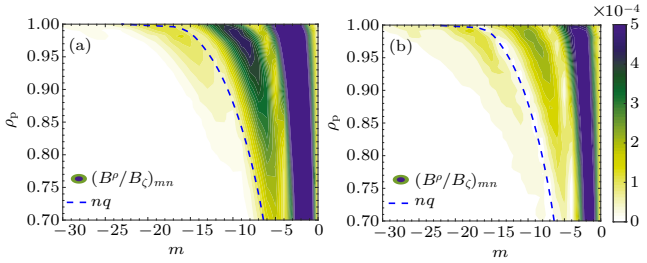


Fig. 4. (a) RMP vacuum field and (b) plasma response field calculated using CLTx. Dashed line indicates the resonant condition $m = nq$, where m is the poloidal mode number (note that the contour plot is drawn based on the data with integer m) and q is the safety factor. ρ_p is the square root of the normalized poloidal flux.

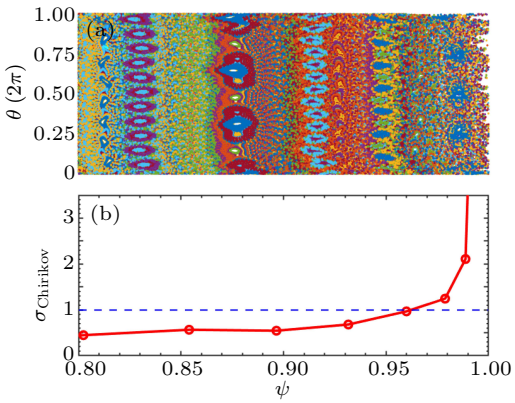


Fig. 5. (a) Poincare plot of the total magnetic field including the response field induced by RMP. (b) The profile of Chirikov parameter $\sigma_{Chirikov}$ along the normalized poloidal magnetic flux.

Figure 4 shows the vacuum field and plasma response field calculated using CLTx according to the EAST experiment with 3-kA RMP coil current. Compared to the vacuum field, the resonant components of the response field are significantly shielded, while some of the non-resonant components are amplified. The corresponding Poincare plot of the total magnetic field including the response field is shown in Fig. 5(a). For this case, the RMP induced stochasticity of the magnetic field is not obvious except for the region at pedestal foot ($\psi > 0.98$), where the Chirikov parameter becomes larger than 1 as shown in Fig. 5(b).

3. Results and discussion

3.1. Radial particle flux

A comparison of the time evolution of the toroidal root-mean-square (RMS) of pressure perturbations at the position of peak pressure gradient in the outer midplane (OMP) is shown in Fig. 6 for the cases with and without RMP. Note that the pressure perturbation δp is normalized by $\bar{n}\bar{T}$, where $\bar{n}$ and $\bar{T}$ are set to 3.32×10^{19} m^{-3} and 1.0 keV respectively. When both cases reach saturation, the pressure perturbation is more intensive when considering RMP, which implies a higher level of turbulence.

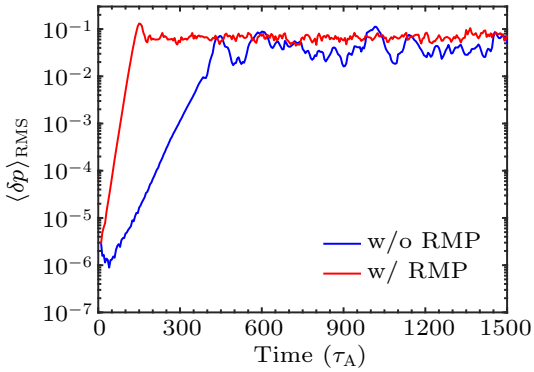


Fig. 6. Time evolution of the toroidal root-mean-square of the normalized pressure perturbations for the case with RMP (red line) and without RMP (blue line). The pressure perturbations are taken from the position of the peak pressure gradient at the outer mid-plane.

It should be noted that, because the response field is directly included in B_0', it acts as an additional driving source and lead to the rapid growth of the perturbations at the initial stage of the nonlinear simulation as shown in Fig. 6. Although it is contrary to the general understanding of the reduction of the growth rate due to RMP,[19,31] similar situation can be seen in several simulation work including RMP fields (e.g., Fig. 4 in Ref. [18] for a BOUT++ simulation and Fig. 4 in Ref. [32] for a gyro-kinetic simulation). To understand the impact of RMP fields on the growth rate, it requires further efforts to perform the simulations based on various profiles (before and after ELM mitigation/suppression) and under RMP fields with different strengths and spectra. Considering the consistency

with the experiment, i.e., the increase in the turbulence intensity and comparable radial particle flux, it can be expected that the simulation is reasonable in the nonlinear saturation phase. Below the nonlinear saturation phase is focused.

When the nonlinear simulations are in the saturation phase, the radial particle flux is calculated by

$$\Gamma_{\rm r} = \left\langle (n_{\rm i0}+n_{\rm i1}) \frac{(\boldsymbol{B}_0 \times \boldsymbol{\nabla}\phi)^{\rm r}}{B_0^2} \right\rangle + \left\langle (n_{\rm i0}+n_{\rm i1}) V_{\|{\rm i}} b_1^{\rm r} \right\rangle . \quad (14)$$

The radial flux includes the $E \times B$ drift flux and the magnetic flutter flux. The fluxsurface average is defined as

$$\langle F \rangle = \frac{\iint Rh_\theta F \,{\rm d}\theta\,{\rm d}\zeta}{\iint Rh_\theta \,{\rm d}\theta\,{\rm d}\zeta}, \quad (15)$$

where $h_\theta = 1/|\nabla\theta|$, R is the major radius. $n_{\rm i0}$ is the equilibrium ion density, while $n_{\rm i1}$ is the perturbed ion density. ϕ is the perturbed electric potential. $V_{\|{\rm i}}$ is the parallel ion velocity. $b_1^{\rm r}$ is the radial component of the magnetic perturbation vector. When calculating the radial flux for the case with RMP, the radial component of the unit vector of the response field $b_{\rm RMP}^{\rm r}$ is also included in the magnetic flutter flux term, i.e., $\left\langle (n_{\rm i0}+n_{\rm i1}) V_{\|{\rm i}} (b_1^{\rm r}+b_{\rm RMP}^{\rm r}) \right\rangle$.

The flux-surface averaged radial particle flux (averaged over 600–1500 $\tau_{\rm A}$) is shown in Figs. 7(a) and 7(b) for the case without and with RMP respectively. For the case without RMP, the turbulence transport is dominated by the $E \times B$ drift flux. For the case with RMP, the $E \times B$ drift flux increases significantly, which is consistent with the increase of perturbation intensity. Meanwhile, the magnetic flutter flux exhibits inward transport when including $b_{\rm RMP}^{\rm r}$ in Eq. (14) (the calculated particle flux related to the $b_1^{\rm r}$ term is still at a similar level with the case without RMP, which has a much lower absolute contribution compared with that for the $b_{\rm RMP}^{\rm r}$ term), which partly offsets the increase of the outward radial flux. While the detailed mechanism of the inward magnetic flutter flux requires further study, a preliminary speculation is proposed as follow. In the region with strong pressure perturbations, when a pressure pattern with higher pressure on the outside and lower pressure on the inside is formed (which is very likely to be encountered due to the existence of the strong outward $E \times B$ drift flux), the pressure induced parallel velocity (see Eq. (3)) could lead to the inward convective flux due to the influence of RMP field on the parallel direction, i.e., $V_{\|{\rm i}} b_{\rm RMP}^{\rm r}$ tends to be negative. Therefore, it would effectively compensate a part of the outward $E \times B$ drift flux. As a result, when including RMP-induced response field, the radial particle flux at the position of peak pressure gradient increases moderately to ~ 1.5 times of that without RMP as shown in Fig. 7(c).

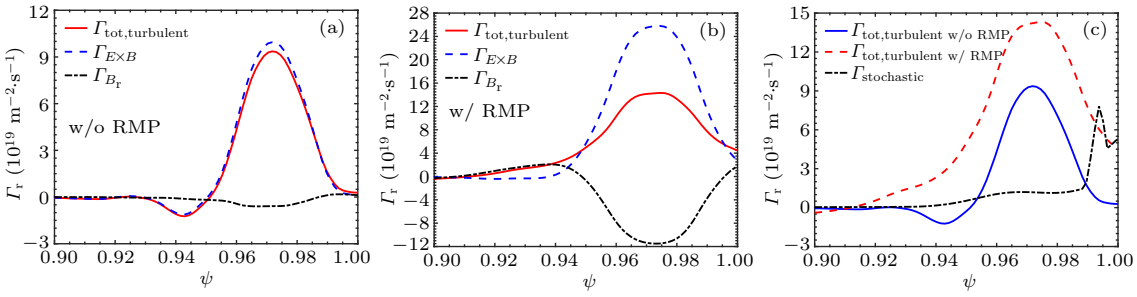


Fig. 7. Profile of the flux-surface averaged radial particle flux (calculated using Eq. (14) and averaged over 600–1500 $\tau_{\rm A}$) for the case (a) without RMP and (b) with RMP. The total raidal flux and the contributions from $E \times B$ drift and magnetic flutter are represented by red solid line, blue dash line and black dash–dot line respectively. The total turbulent transprt flux are compred in panel (c) between the case without RMP (blue solid line) and with RMP (red dash line). The transport due to stochastic fields is also shown by black dash–dot line.

To provide a preliminary comparison of the radial particle transport induced by the turbulence and the stochastic magnetic field, the radial flux driven by the stochastic magnetic field is further shown in Fig. 7(c) by the black dash–dot line, which is roughly estimated by[10,33]

$$\Gamma_{\rm stochastic} \approx -C_{\rm s} D_{\rm FL} \,{\rm d}n_{\rm i}/{\rm d}r, \quad (16)$$

where $C_{\rm s} = \sqrt{(T_{\rm e}+T_{\rm i})/m_{\rm i}}$ is the ion sound velocity and

$$D_{\rm FL} = \pi q R \sum\nolimits_{m,n} \left((B_{\rm r}/B_0)_{m,n} \right)^2 \delta(m/q - n) \quad (17)$$

is the diffusion coefficient of magnetic fields along the field line. As mentioned in Subsection 2.3, the stochasticity of the magnetic field is weak for the case studied in this work. Therefore, no significant radial flux is induced in the pedestal region until approaching the separatrix ($\psi > 0.99$) when the Chirikov parameter is much larger than 1.

To estimate the radial flux in the experiment, an SOLPS-ITER[34,35] simulation is performed based on our previous work.[36–39] The density, ion/electron temperature at the core-edge interface is fixed and the transport coefficients are adjusted to match the experimental profiles in the SOLPS-ITER simulation. The estimated flux-surface averaged radial particle flux is $\sim 1.8 \times 10^{20}$ m^{-2}·s^{-1} at the position of peak pressure gradient. The enhanced turbulence transport due to RMP is well consistent with the estimated radial flux, which implies that the turbulence transport could have a dominating contribution to the radial flux in the RMP induced ELM suppression phase, especially for the case without significant stochasticity of the magnetic field.

3.2. Mechanism of enhanced transport

In this section, the mechanism of the enhanced transport is further analyzed. We focus on the $E \times B$ drift flux because it dominates the outward radial particle flux. The electric drift flux can be also estimated approximately as the sum of the contributions from individual modes with different toroidal mode number n, i.e.,

$$\langle \Gamma_{\rm r} \rangle_\zeta \approx \frac{2}{RB_{\rm P}} \sum_{n=1}^{\infty} n \left| n_{{\rm i},n} \right| \left| \phi_n \right| \sin(\varphi_{n_{\rm i}} - \varphi_\phi), \tag{18}$$

where the radial transport flux due to an individual mode is proportional to the amplitudes of the Fourier components of the density perturbation $n_{{\rm i},n}$ and the potential perturbation ϕ_n. The radial transport flux is also modulated by the phase difference between the density and electric potential perturbations $\delta\varphi = \varphi_{n_{\rm i}} - \varphi_\phi$. When the phase difference (in the range of $(-\pi, \pi)$) is greater/lower than 0, the particle flux is directed radially outward/inward. Below, the effect of RMP on the mode amplitude and phase difference is investigated at the position of peak pressure gradient in the OMP, where the outward particle flux has the peaked value.

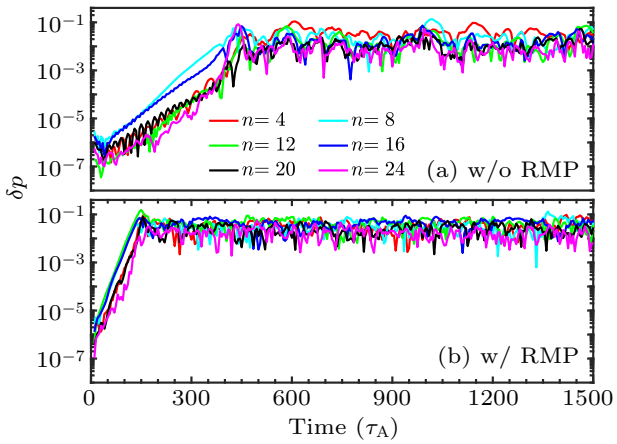


Fig. 8. Time evolutions of normalized pressure perturbations for different toroidal modes for the case (a) without RMP and (b) with RMP. The pressure perturbations are taken from the position of the peak pressure gradient at the OMP.

The time evolutions of the pressure perturbations for modes with different n are shown in Figs. 8(a) and 8(b) for the case without and with RMP, respectively. The corresponding time evolutions of normalized toroidal mode spectra are shown in Fig. 9. While the $n = 4$ mode dominates for the case without RMP accompanied with intermittent burst of multiple modes, more broad distribution can be found around $n = 16$ mode for the case with RMP. The mode–mode nonlinear coupling strength is further evaluated using an autocorrelation spectrum analysis method,[40,41] as shown in Fig. 10 during the nonlinear saturation phase. For the case without RMP shown in Fig. 10(a), it can be seen that strong coupling strength exists between the $n = 4$, 8, 12, 16 modes. Thus, while the detailed mechanism requires further investigation, it is believed that the $n = 4$ mode gains energies and becomes dominating due to the nonlinear interaction. Compared to the case without RMP, the region of high coupling strength (red color) in the autocorrelation spectrum for the case with RMP is obviously enlarged, and the average coupling strength is also increased. Thus, it can be understood that the enhanced multi-mode coupling effectively promotes the redistribution of perturbation energy in the spectral space. The enhanced interaction of PBMs is consistent with previous findings.[26,42]

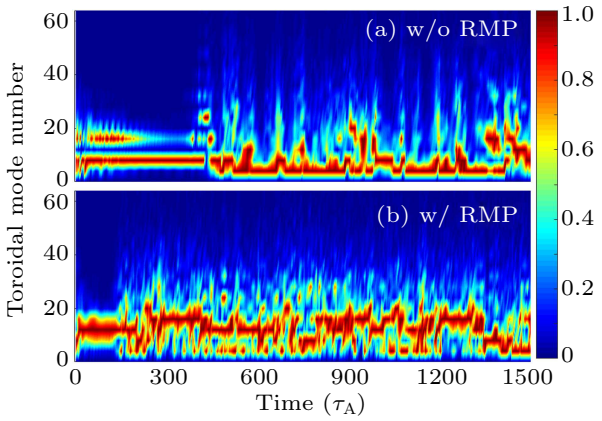


Fig. 9. Time evolution of the normalized toroidal mode spectrum of pressure perturbations for the case (a) without RMP and (b) with RMP. The pressure perturbations are taken from the position of the peak pressure gradient at the OMP.

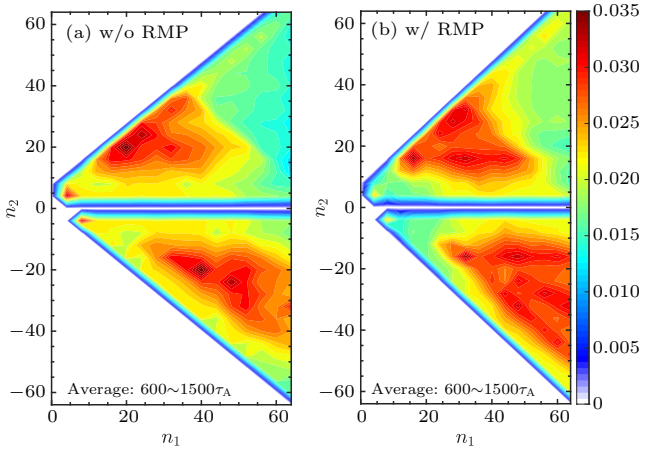


Fig. 10. Autocorrelation spectrum of pressure perturbations averaged over 600–1500 $\tau_{\rm A}$ for the case (a) without RMP and (b) with RMP. The pressure perturbations are taken from the position of the peak pressure gradient at the OMP.

The amplitudes of ion density and electric potential perturbations are shown in Fig. 11. The overall increase of the amplitudes for the case with RMP indicates the increase of turbulence intensity. The reduction of the amplitude of $n = 4$ density perturbation at the position of peak pressure gradient may be related to the radial broadening of the mode structure due to the RMP field, which needs further work to explore the detailed mechanism. It can be also seen that, rather than the monotonic decrease in the amplitude of density perturbation with increasing n, a peak appears at $n = 16$ for the case with RMP. The comparison of the phase difference $\delta\varphi$ between the

density and electric potential perturbations for $n = 16$ mode is further shown in Fig. 12(a). The phase differences for the case with RMP are more likely to distribute near $\pi/2$, which facilities the outward radial transport according to Eq. (18). According to the phase difference and the peak around $k_\theta \rho_s \sim 0.2$ (where k_θ is the poloidal wavenumber and ρ_s is the hybrid Larmor radius) at the direction of ion diamagnetic drift in the poloidal wavenumber–frequency power spectral (not shown here), it is suspected that the kinetic-ballooning-mode (KBM) turbulence dominates the radial transport for the case with RMP. The destabilizing of KBM (plasma-beta $\sim 0.3\%$) may relate to the RMP-induced change in the local magnetic shear or curvature,[43] which needs further study in future. The time-averaged sine of $\delta\varphi$ over 600–1500 τ_A for various n are shown in Fig. 12(b). The effect on enhancing transport for the case with RMP due to the change in phase difference can be reflected for the medium-n modes. It should be noted that, it does not exactly correspond to the radial transport, which is proportional to the product of the perturbation amplitudes and the sine of phase difference.

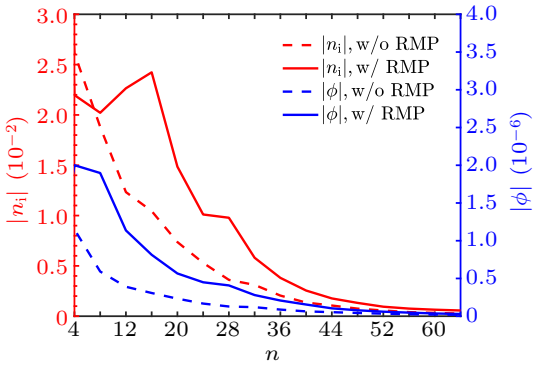


Fig. 11. The amplitudes (averaged over 600–1500 τ_A) of density (red color) and potential (blue color) perturbations with different toroidal mode numbers for the cases with (solid lines) and without RMP (dash lines).

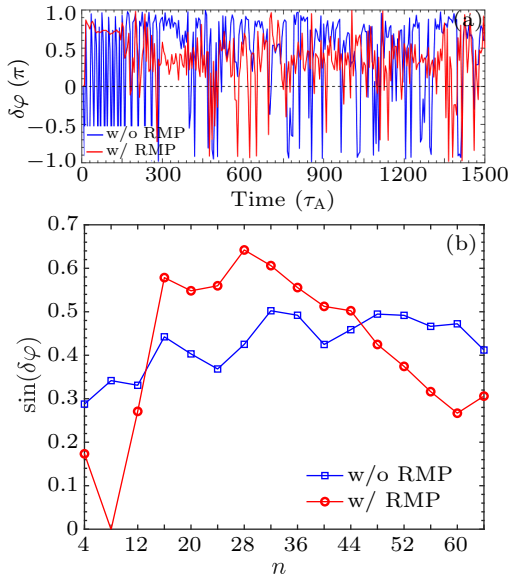


Fig. 12. (a) Time evolution of the phase difference between the $n = 16$ density and electric potential perturbations and (b) the time-averaged (600–1500 τ_A) sine of phase difference of various toroidal modes for the case with RMP (red line) and without RMP (blue line).

The radial particle fluxes Γ_n for various toroidal modes are shown in Fig. 13. When RMP induced response field is considered, the enhancement in the radial particle flux corresponds to the increased contributions from the toroidal modes with $n \geq 12$, which is mainly due to the increase in the perturbation amplitudes. The change in phase difference can further enhance the contribution from medium n modes, but reduce the radial flux especially for the modes with $n = 4$ and 8. As a result, the radial particle transport is dominated by $n = 12$, 16, 20 modes for the case with RMP, while for the case without RMP, $n = 4$, 8, 12 modes dominate.

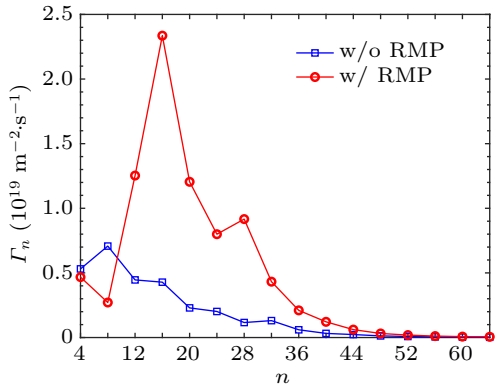


Fig. 13. The radial particle flux (calculated by Eq. (18), averaged over 600–1500 τ_A) of various toroidal modes for the case with RMP (red line) and without RMP (blue line).

3.3. Change in Jensen–Shannon complexity

The complexity–entropy analysis[44] is capable to characterize the turbulence behavior.[45,46] Recently, Choi *et al.*[47] has applied the complexity–entropy analysis to investigate the characteristics of edge plasma temperature fluctuation in KSTAR experiment of ELM suppression by RMP. It was found that, during RMP-induced ELM suppression phase, the Jensen–Shannon complexity[44] is reduced while the strength of bicoherence is increased. Based on a multi-scale model of quasi-mode evolution in a stochastic magnetic field, Cao *et al.*[48] indicated that the correlation between the micro-turbulence and the stochastic magnetic field induced by RMP responses for the reduction of Jensen–Shannon complexity of edge plasma fluctuation, which becomes more stochastic or "nosiy". For the simulated edge plasma fluctuations, the Jensen–Shannon complexity is calculated to characterize the effect of RMP on the turbulence behavior.

Jensen–Shannon complexity (C_{JS}) is defined as the product of the permutation entropy (H) and Jensen–Shannon divergence (Q),[44] i.e.,

$$C_{JS} = HQ, \tag{19}$$

where H reflects the degree of information loss in the system, and Q characterizes the statistical distance of the system from thermal equilibrium. The calculated C_{JS} values align with intuitive perceptions of system complexity. Within the Jensen–Shannon–complexity framework, both white noise and perfect

crystals represent "simple" systems. Specifically, white noises exhibit high entropy but low complexity due to the absence of discernible structure, while perfect crystals have both low entropy and low complexity owing to their perfectly regular structure.

The Jensen–Shannon complexity ($C_{\rm JS}$) is calculated for the simulated plasma density fluctuations as follows. Within a window of length d, the segment can be taken from the sequential data, i.e., the time evolution of the simulated plasma parameters. In this work, d is chosen as 3 due to the limited number of data points. For the data segment denoted by (a_1, a_2, a_3), the permutation can be obtained according to the order of the values. For example, if $a_2 < a_1 < a_3$, the permutation is (1, 0, 2). There is totally $d!$ ($3! = 6$) possible permutations. By sliding the window along the sequential data, the probability distribution P can be obtained according to the probability of each possible permutation:

$$P = \{p_1, p_2, \ldots, p_{d!}\}. \tag{20}$$

The Shannon entropy H is then calculated by

$$H = \frac{S(P)}{S_{\max}}, \tag{21}$$

where

$$S(P) = -\sum_{i=1}^{d!} p_i \log(p_i), \tag{22}$$

and $S_{\max} = \log(d!)$ is the entropy of the uniform distribution $P_{\rm e} = \{P_i = 1/d!\}$. The Jensen–Shannon divergence Q is defined as

$$Q = Q_0 \left\{ S\left[(P + P_{\rm e})/2\right] - S[P]/2 - S[P_{\rm e}]/2 \right\}, \tag{23}$$

where Q is the normalization constant.

After including RMP field, the Jensen–Shannon complexity of plasma density fluctuations is reduced, as shown Fig. 14. Considering the increase in the bicoherence as indicated in Fig. 10, the simulated results show a similar trend with the experimental observation by Choi *et al.*[47] The decrease of the complexity is accompanied with an increase in the entropy, which implies that the RMP fields would lead the edge plasma turbulence more stochastic or "nosiy" as mentioned above. According to the present results, it could relate the more stochastic turbulence behavior to enhanced mode-mode coupling due to the RMP field, i.e., stronger nonlinear interactions between toroidal modes lead the mode spectra broader and therefore the fluctuations more stochastic. It should be noted that, this is a preliminary finding based on the comparison between the simulation cases with and without RMP induced response field for the profiles during the ELM suppression phase. Further work should be conducted for different ELM situations by a systematic complexity–entropy analysis to understaned the detailed influence of RMP field on the turbulence behavior and corresponding physical mechansim.

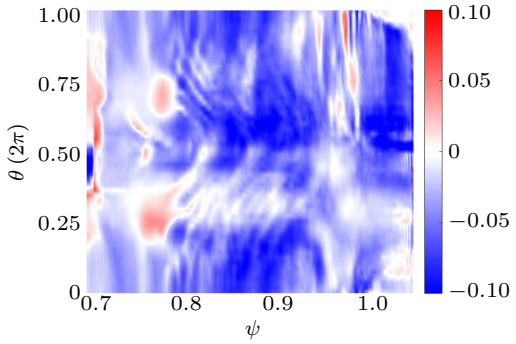


Fig. 14. Changes of the complexity of the density fluctuations after introducing RMP induced response filed.

4. Summary

Based on the BOUT++ six-field two-fluid model, the influence of RMP on edge plasma turbulent transport during ELM suppression phase is investigated. According to the profiles during the ELM suppression phase in EAST experiment with $n = 4$ RMP, the plasma response field is calculated using CLTx and introduced in the BOUT++ simulations.

The flux-surface averaged radial particle flux at the position of peak pressure gradient is found to be increased by a factor of $\sim 50\%$ for the case with RMP. It is the result of the significant enhanced turbulent electric drift flux, which is partly offset by inward magnetic flutter flux. Due to the weak stochasticity of the magnetic field for the studied case, the radial flux driven by the stochastic field is not significant until approaching the separatrix ($\psi > 0.99$). The enhanced turbulent flux is consistent with the radial particle flux estimated by SOLPS-ITER simulation according to the experimental profiles, which implies that the turbulent transport could have a dominating contribution to the radial transport for maintaining the pedestal density profile during ELM suppression phase after density pump-out. The enhancement of the radial particle flux corresponds to the increasing contributions of the $n \geq 12$ toroidal modes, which is mainly due to the enhanced plasma density and electric potential perturbations. The change in the phase difference between them also facilitates the outward radial transport for the medium-n modes, but suppresses the contributions of low-n modes. As a result, the contributions of $n = 12$, 16, 20 modes dominate the radial particle flux for the case with RMP, while $n = 4$, 8, 12 modes for the case without RMP.

A preliminary complexity–entropy analysis is performed on the simulated plasma density perturbations to characterize the influence of RMP field on the turbulence behavior. The reduction in the complexity and increase of the entropy suggests that the turbulence becomes more stochastic, which is consistent with the previous experimental and theoritical study.

The change in the turbulence characteristic could be related to the enhanced mode-mode coupling and thus broadened mode spectra due to the RMP effect, which provides a possible explanation for the experimental observation of simultaneous decrease of the complexity and increase of the bicoherence.

It has been pointed out by Seto *et al.*[29] that low n perturbations may play a significant role in the plasma response to RMP, and a high-frequency $n = 1$ mode has been observed during ELM suppression phase in EAST RMP experiment.[14] Due to the deficiency of the simulation based on 1/4 torus in this work, the interaction with $n = 1$ mode has not been captured. To understand the role of the $n = 1$ mode, the full-torus simulation will be conducted in the future work. Furthermore, for further investigating the contribution of turbulence transport during the density pump-out induced by RMP, the simulation work will be performed based on the profiles before ELM suppression.

Acknowledgements

Project supported by the National MCF Energy Research and Development Program of China (Grant Nos. 2024YFE03010003, 2019YFE03080500, and 2019YFE03030004). The results are obtained with the help of the EIRENE package (see www.eirene.de) including the related code, data, and tools.[49] Numerical simulations are carried out using the CFETR Integration Design Platform (CIDP)[50,51] with the support of the Supercomputing Center of University of Science and Technology of China.

References

[1] Sun Y, Ma Q, Jia M, Gu S, Loarte A, Liang Y, Liu Y Q, Paz-Soldan C A, Wu X M, Xie P C, Ye C, Wang H H, Zhao J Q, Guo W, He K, Li Y Y, Li G, Liu H, Qian J, Sheng H, Shi T, Wang Y M, Weisberg D, Wan B, Zang Q, Zeng L, Zhang B, Zhang L, Zhang T, Zhou C and Contributors E 2021 *Nuclear Fusion* **61** 106037
[2] Lanctot M J, Buttery R J, De Grassie J S, Evans T E, Ferraro N M, Hanson J M, Haskey S R, Moyer R A, Nazikian R, Osborne T H, Orlov D M, Snyder P B, Wade M R and The D D T 2013 *Nuclear Fusion* **53** 083019
[3] Suttrop W, Kirk A, Bobkov V, Cavedon M, Dunne M, Mcdermott R M, Meyer H, Nazikian R, Paz-Soldan C, Ryan D A, Viezzer E, Willensdorfer M, The A U and Teams M S T 2018 *Nuclear Fusion* **58** 096031
[4] Suttrop W, Kirk A, Nazikian R, Leuthold N, Strumberger E, Willensdorfer M, Cavedon M, Dunne M, Fischer R, Fietz S, Fuchs J C, Liu Y Q, Mcdermott R M, Orain F, Ryan D A, Viezzer E, The A U T, The D-D T and The Eurofusion M S T T 2017 *Plasma Physics and Controlled Fusion* **59** 014049
[5] Team K, Jeon Y M, Park J K, Yoon S W, Ko W H, Lee S G, Lee K D, Yun G S, Nam Y U, Kim W C, Kwak J G, Lee K S, Kim H K and Yang H L 2012 *Phys. Rev. Lett.* **109** 035004
[6] Wang S X, Liu H Q, Jie Y X, Ding W X, Zeng L, Sun Y W, Lian H, Zhu X, Zou Z Y, Lyu B, Li Y Y, Zang Q, Du H F, Zhou C, Liu A D, Zhang T, Gao W, Gao X and The E T 2018 *Nuclear Fusion* **58** 112013
[7] Hu Q M, Nazikian R, Grierson B A, Logan N C, Paz-Soldan C and Yu Q 2020 *Nuclear Fusion* **60** 076001
[8] Leuthold N, Suttrop W, Willensdorfer M, Birkenmeier G, Brida D, Cavedon M, Dunne M, Conway G D, Fischer R, Gil L, Happel T, Hennequin P, Kappatou A, Kirk A, Manz P, Mcdermott R M, Vicente J, Zohm H, Upgrade Team T A and Mst1 Team T E 2023 *Nuclear Fusion* **63** 046014
[9] Sun Y, Jia M, Zang Q, Wang L, Liang Y, Liu Y Q, Yang X, Guo W, Gu S, Li Y, Lyu B, Zhao H, Liu Y, Zhang T, Li G, Qian J, Xu L, Chu N, Wang H H, Shi T, He K, Chen D, Shen B, Gong X, Ji X, Wang S, Qi M, Yuan Q, Sheng Z, Gao G, Song Y, Fu P, Wan B and Contributors E 2017 *Nuclear Fusion* **57** 036007
[10] Chang Y, Sun Y, Sheng H, Yan X, Li H, Xie P, Zhang W, Guo J, Mao S, Liu Y, Zhang L, Duan Y, Li Y, Zang Q and Ye M 2023 *Physics of Plasmas* **30** 122301
[11] Zhang N, Liu Y Q, Yu D L, Liu Y, Hao G Z, Liu L, He X X, Sun T F, Ji X Q, Wang S, Dong G Q, Bai X, Wei Y L, Chen W J, Sun Y W, Jiang M, Zhang Y P, Shi Z B, Zhong W L and Xu M 2023 *Nuclear Fusion* **63** 086019
[12] Liu Y, Kirk A, Gribov Y, Gryaznevich M P, Hender T C and Nardon E 2011 *Nuclear Fusion* **51** 083002
[13] Paz-Soldan C, Nazikian R, Haskey S R, Logan N C, Strait E J, Ferraro N M, Hanson J M, King J D, Lanctot M J, Moyer R A, Okabayashi M, Park J K, Shafer M W and Tobias B J 2015 *Phys. Rev. Lett.* **114** 105001
[14] Liu S C, Liang Y, Li L T, Tang T F, Wu X H, Yan N, Shi T H, Li G S, Ye K X, Meng L Y, Ding R, Sun Y, Jia M, Ma Q, Zang Q, Li X, Wang S X, Wang M R, Zhao H L, Wei J L, Zhang T, Jin Y F, Liao L, Wei W Y, Li Y, Chen R, Hu G H, Zhao N, Liu X J, Ming T F, Han X, Zhang W B, Wang L, Qian J P, Zeng L, Li G Q, Xu G S, Gong X Z, Gao X and The E T 2023 *Nuclear Fusion* **63** 042003
[15] Wilcox R S, Shafer M W, Ferraro N M, Mckee G R, Zeng L, Rhodes T L, Canik J M, Paz-Soldan C, Nazikian R and Unterberg E A 2016 *Phys. Rev. Lett.* **117** 135001
[16] Mckee G R, Yan Z, Holland C, Buttery R J, Evans T E, Moyer R A, Mordijck S, Nazikian R, Rhodes T L, Schmitz O and Wade M R 2013 *Nuclear Fusion* **53** 113011
[17] Dudson B D, Umansky M V, Xu X Q, Snyder P B and Wilson H R 2009 *Comput. Phys. Commun.* **180** 1467
[18] Kim J, Kim S S and Jhang H 2019 *Nuclear Fusion* **59** 096019
[19] Dong L K, Chen S Y, Mou M L, Luo Y, Qin C C and Tang C J 2023 *Nuclear Fusion* **63** 086023
[20] Dong L, Chen S, Mou M and Tang C 2020 *Plasma Science and Technology* **22** 115101
[21] Dong L, Chen S, Mou M, Luo Y, Qin C and Tang C 2024 *Plasma Science and Technology* **26** 015102
[22] Deng C, Liu Z, Xia T, Liu Y, Li P, Long F, Gao X, Wang S, Li G, Liu H, Zang Q, Li J, Yang K, Wu M, Yin X, Li H, Xie J, Lan T, Mao W, Liu A, Zhou C, Ding W, Zhuang G, Liu W and The E T 2024 *Plasma Science and Technology* **26** 065103
[23] Wang X, Zhang H W, Chen W J, Sun T F, Zhang W and Ma Z W 2023 *Nuclear Fusion* **63** 096023
[24] Jia M, Loarte A, Sun Y, Ma Q, Wu X, Xie P, Gu S, Hou J, He K, Li G, Li K, Li Y, Liang Y, Paz-Soldan C, Shi T, Shen B, Wan B, Wang H, Wang L, Wang Y, Xu J, Xu S, Yang Z, Zang Q, Zhang B, Zhang J, Zhang L and Zuo G 2021 *Nuclear Fusion* **61** 106023
[25] Xia T Y, Xu X Q and Xi P W 2013 *Nuclear Fusion* **53** 073009
[26] Kim S K, Pamela S, Kwon O, Becoulet M, Huijsmans G T A, In Y, Hoelzl M, Lee J H, Kim M, Park G Y, Kim H S, Lee Y H, Choi G J, Lee C Y, Kirk A, Thornton A, Team J and Na Y S 2020 *Nuclear Fusion* **60** 026009
[27] Wu X M, Sun Y, Ma Q, Gu S, Wang Y F, Geng K N, Zhang X X, Li G Q, Sheng H, Zhang T, Snyder P B, Zhang Q, Qian J, Li Y Y and Wan B 2025 *Nuclear Fusion* **65** 076031
[28] Dudson B D, Allen A, Breyiannis G, Brugger E, Buchanan J, Easy L, Farley S, Joseph I, Kim M, Mcgann A D, Omotani J T, Umansky M V, Walkden N R, Xia T and Xu X Q 2015 *Journal of Plasma Physics* **81** 365810104
[29] Seto H, Dudson B D, Xu X-Q and Yagi M 2023 *Comput. Phys. Commun.* **283** 108568
[30] Wang S and Ma Z W 2015 *Physics of Plasmas* **22** 122504
[31] Bécoulet M, Orain F, Huijsmans G T A, Pamela S, Cahyna P, Hoelzl M, Garbet X, Franck E, Sonnendrücker E, Dif-Pradalier G, Passeron C, Latu G, Morales J, Nardon E, Fil A, Nkonga B, Ratnani A and Grandgirard V 2014 *Phys. Rev. Lett.* **113** 115001
[32] Hager R, Chang C S, Ferraro N M and Nazikian R 2020 *Physics of Plasmas* **27** 062301
[33] Tokar M Z 1997 *Fusion Engineering and Design* **37** 417
[34] Wiesen S, Reiter D, Kotov V, Baelmans M, Dekeyser W, Kukushkin A S, Lisgo S W, Pitts R A, Rozhansky V, Saibene G, Veselova I and Voskoboynikov S 2015 *Journal of Nuclear Materials* **463** 480
[35] Bonnin X, Dekeyser W, Pitts R, Coster D, Voskoboynikov S and Wiesen S 2016 *Plasma and Fusion Research* **11** 1403102

[36] Guo J, Lu Z, Jia G, Ruan X, Xu Y, Mao S, Yang J, Wang Y, Meng L, Yang Q, Xu G and Ye M 2021 *Plasma Physics and Controlled Fusion* **63** 125006
[37] Guo J, Mao S, Jia G, Meng L, Li A, Xu J, Xu G and Ye M 2022 *Nuclear Fusion* **62** 126051
[38] Guo J, Xu Y, Mao S and Ye M 2023 *Nuclear Fusion* **63** 126033
[39] Guo J, Mao S, Meng L, Xu G, Ding R and Ye M 2024 *Nuclear Fusion* **64** 106004
[40] Holland C, Tynan G R, Diamond P H, Moyer R A and Burin M J 2002 *Plasma Physics and Controlled Fusion* **44** A453
[41] Kim Y C and Powers E J 1978 *Physics of Fluids* **21** 1452
[42] Kim S K, Pamela S, Logan N C, Na Y S, Lee C Y, Park J K, Yang S M, Hu Q, Becoulet M, Huijsmans G, Hoelzl M, In Y, Kim M W, Lee H H, Lee J, Lee J H, Kwon O, Kolemen E and The J T 2022 *Nuclear Fusion* **62** 106021
[43] Willensdorfer M, Cote T B, Hegna C C, Suttrop W, Zohm H, Dunne M, Strumberger E, Birkenmeier G, Denk S S, Mink F, Vanovac B, Luhmann L C and The A U T 2017 *Phys. Rev. Lett.* **119** 085002
[44] Rosso O A, Larrondo H A, Martin M T, Plastino A and Fuentes M A 2007 *Phys. Rev. Lett.* **99** 154102
[45] Zhu Z, White A E, Carter T A, Baek S G and Terry J L 2017 *Physics of Plasmas* **24** 042301
[46] Maggs J E, Rhodes T L and Morales G J 2015 *Plasma Physics and Controlled Fusion* **57** 045004
[47] Choi M J, Kwon J M, Kim J, Rhee T, Bak J G, Shin G, Kim H S, Jhang H, Kim K, Yun G S, Kim M, Kim S, Kaang H H, Park J K, Lee H H, In Y, Lee J, Kim M, Park B H and Park H K 2022 *Physics of Plasmas* **29** 122504
[48] Cao M and Diamond P H 2024 *Nuclear Fusion* **64** 036003
[49] Reiter D, Baelmans M and Boerner P 2005 *Fusion Science and Technology* **47** 172
[50] Ye M, Wang Z, Mao S, Song Y, Liu X, Chan V and Li J 2017 *Fusion Engineering and Design* **123** 87
[51] Mao S, Ye M, Li Y, Zhang J, Zhan X, Wang Z, Xu K, Liu X and Li J 2019 *Fusion Engineering and Design* **146** 1153